

Evidence of magnetite reduction and primary magnetization destruction during early diagenesis in sediments from Maldives Inner Sea

Igor Gustavo da Fonseca Carrasqueira^{1,*} , Luca Lanci² , Luigi Jovane¹ 

¹ Departamento de Oceanografia Física – Instituto Oceanográfico da Universidade de São Paulo (Praça do Oceanográfico, 191 – São Paulo – SP – Brazil – 05.508-120).

² Department of Pure and Applied Science – University of Urbino (Via S. Chiara, 27 – Urbino – Italy – 61.029).

* Corresponding author: igor.carrasqueira@usp.br

ABSTRACT

Magnetic experiments have provided insight into the preservation of magnetite in sediments of the Inner Sea of the Maldives during early diagenesis. In this study, we present high-resolution remanence data on the upper 15 meters of the sedimentary record and a detailed magnetic characterization of discrete samples from the top 5.5 meters of the International Ocean Discovery Program (IODP) Site U1471 record. Based on magnetic experiments, it can be concluded that magnetite is rapidly reduced, with a large decrease in natural remanent magnetization (NRM) related to destruction of primary NRM below the upper two meters of the sedimentary record. In thermomagnetic experiments, the appearance of a greigite signal at 3.06 meters below sea floor (mbsf) suggests that current diagenesis could imprint nearly 100 kyr of error on the chronology based on magnetostratigraphy. Furthermore, based on X-ray fluorescence data, it can be concluded that magnetite reduction did not affect the Fe record.

Keywords: IODP exp. 359, Indian Ocean, Magnetostratigraphy, Carbonate platform, Siderite

INTRODUCTION

Geomagnetic data is a powerful tool widely used to improve record chronology. These data make it possible to correlate records using a worldwide synchronous parameter. In marine sedimentary records, natural remanent magnetization (NRM) is mainly carried by magnetite (Fe_3O_4), and its record is almost synchronous with the period of sediment deposition (Ogg, 2020).

However, under certain conditions, magnetite can interact with living organisms and/or environmental geochemistry, changing its oxidation state and destroying primary magnetization (Rowan and Roberts, 2006, 2005; Rowan et al., 2009; Rodelli et al., 2019, 2018).

Under anoxic conditions, iron-bearing minerals such as magnetite react with H_2S , produced by the bacterial reduction of sulphate during the decomposition of organic matter, forming pyrite (FeS_2) (Berner, 1984; Rowan and Roberts, 2006; Rowan et al., 2009; Rodelli et al., 2019). Pyritization occurs by a series of mineral precursors that also include greigite (Fe_3S_4) (Berner, 1984; Wilkin and Barnes, 1997; Rowan and Roberts, 2006; Rowan et al., 2009; Rodelli et al., 2019). It has been

Submitted: 27-Jul-2023

Approved: 23-Dec-2023

Editor: Rubens Lopes



© 2024 The authors. This is an open access article distributed under the terms of the Creative Commons license.

suggested that where reactive iron is abundant and organic carbon is relatively restricted, any dissolved sulphide reacts rapidly with the available dissolved iron, leading to incomplete pyritization and the preservation of greigite (Kao et al., 2004; Dantas et al., 2022).

According to Berner's steady-state diagenetic model (Berner, 1984), pyritization reactions are confined to the top of the sedimentary column, therefore, any remanence carried by authigenic greigite formed during early reductive diagenesis will record the geomagnetic field close to the time of sediment deposition, without substantial delay. However, increasing reports of later greigite formation indicate that greigite can form at any time after deposition (Florindo and Sagnotti, 1995; Jiang et al., 2001; Roberts and Weaver, 2005; Sagnotti et al., 2005). If the greigite is a remanence carrier in a sedimentary record, the possibility that the paleomagnetic record has been compromised by delayed remanence acquisition must be considered (Rowan and Roberts, 2006). Greigite shares some magnetic properties with magnetite, such as the saturation of isothermal remnant magnetization (SIRM) and coercivity (Roberts et al., 2011). The SIRM of greigite is typical of ferrimagnets such as magnetite, in which SIRM is reached at applied fields of <0.3 T (Roberts et al., 2011). These shared properties make it difficult to differentiate a primary NRM carried by magnetite from a secondary NRM carried by greigite using Alternating Flow (AF) demagnetization, because the coercivity spectra overlap.

In the sedimentary records of the Inner Sea of the Maldives, where the chronology based on biostratigraphy has a poorly constrained age due to a discrepancy of up to about 500 Kyr between nannofossil and planktonic foraminifers (Betzler et al., 2017a, 2018), a chronology based on magnetostratigraphy is preferred. However, the Maldives archipelago is under the seasonal influence of the Arabian Sea Oxygen Minimum Zone (OMZ), which forms in the north of the Arabian Sea at 200 to 1,200 m depth (Reid, 2003; Stramma et al., 2008) in response

to wind-driven upwelling during the summer monsoon. The lateral expansion of the Arabian Sea OMZ towards the tropics reaches low oxic values at 500 to 1,000 m depth in the Maldives region (Weiss et al., 1983; Reid, 2003; Bunzel et al., 2017). Its influence on the archipelago dates back to the Miocene (Betzler et al., 2016).

The procedures of the International Ocean Discovery Program (IODP) for Site U1471 (Betzler et al., 2017a) tentatively constructed a chronology based on the magnetostratigraphy for the upper 180 mbsf in Hole U1471C. Nevertheless, the poor quality of the data places large uncertainties on the magnetostratigraphy. In addition, the occasional presence of pyrite has been noted (Betzler et al., 2017a, 2017b).

Although these data suggest that the sediment was under reducing conditions, to date, no studies have been carried out on the preservation of magnetite and, consequently, on the preservation of the geomagnetic record in sediments of the Inner Sea of the Maldives during early diagenesis.

MALDIVES SETTING

The Maldives archipelago, located in the central equatorial Indian Ocean, is an isolated tropical carbonate platform and makes up most of the central part of the Chagos-Laccadives Ridge, which lies to the southwest of India (Figure 1). The double line of atolls oriented from north to south includes the Inner Sea of the Maldives. These atolls are separated from each other by channels that deepen towards the Indian Ocean (Purdy and Bertram, 1993). The Inner Sea is an internal basin with a water depth of up to 550 meters. It is characterized by the deposition of periplatform oozes (Droxler, 1990; Malone et al., 1990), accumulated locally in sediment-drift bodies (Betzler et al., 2009).

The sediments that accumulate in the Inner Sea of the Maldives are mainly composed of the pelagic test of foraminifera, pteropods and coccolithophores (mostly calcite and some aragonite) associated with fine bank-derived neritic carbonate particulates (mostly aragonite

and some magnesian calcite); their variations over time reflect changes in equatorial Indian Ocean currents, upwelling, dust fertilization and global sea level (Betzler et al., 2009, 2013a, 2013b, 2017a). These sediments are also composed of a minor lithogenic fraction dominated by fine particles (Lindhorst et al., 2019). This lithogenic fraction has previously been associated with aeolian dust transported from the deserts of the

Indian-Asian landmass by dry north-easterly winds during the winter monsoon (Bunzel et al., 2017; Kunkelova et al., 2018). Their contribution to the Inner Sea of the Maldives has been linked to the extension of arid zones on the Indian-Asian landmass, which evolves in response to the ~100 kyr cyclicity in global ice volume (Bunzel et al., 2017; Kunkelova et al., 2018; Carrasqueira et al., 2023).

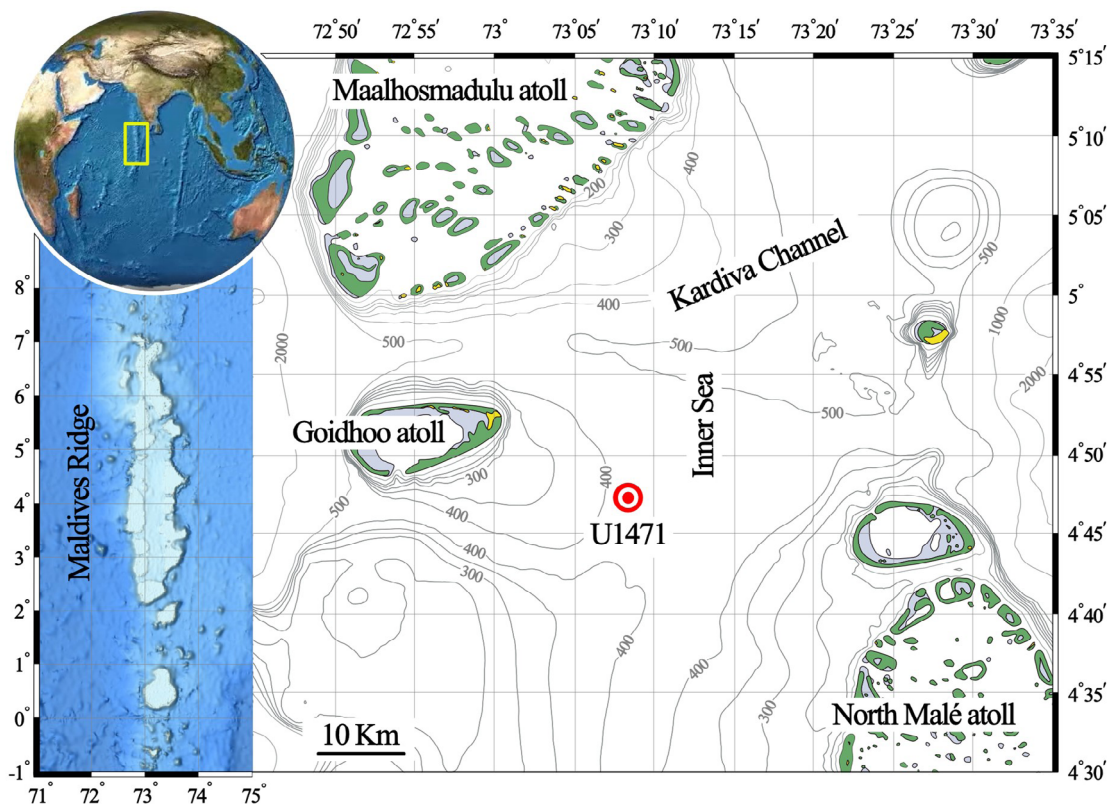


Figure 1. Location of the Maldives Archipelago (yellow rectangle) along the central part of the Chagos-Laccadives Ridge in the Indian Ocean. Site U1471 is located in the deepest part of the Inner Sea, near the outflow of the southern branch of the Kardiva Channel into the Inner Sea (adapted from Betzler et al., 2017a).

Located in the deepest part of the Inner Sea, where the seafloor is essentially flat, IODP Site U1471 (4°45.98'N and 73°08.11'E; Figure 1) is at a water depth of 419.3 meters, near the outflow of the southern branch of the Kardiva Channel into the Inner Sea. The lithology in the studied interval was characterized by unlithified, well-preserved planktonic foraminifer-rich, fine- to medium-grained packstone to wackestone (Betzler et al., 2017a).

METHODS

In cubic samples with a volume of 8 cm³ collected from the core of Site U1471, Anhyseretic Remanent Magnetization (ARM) was measured in the upper 15 mbsf and detailed magnetic experiments were made in the upper 5.5 mbsf. ARM and isothermal remnant magnetization (IRM) experiments were also measured continuously (every 1 cm) in 11 U-channels, comprising the upper 15 mbsf. X-ray

fluorescence (XRF) was measured in a continuous record (1 cm resolution) from 11 half-core sections collected in the upper 15 mbsf, and 41 discrete samples were measured on conventional benchtop XRF collected from core section U1471C-1H-3W.

NATURAL REMANENT MAGNETIZATION (NRM)

To investigate the structure of NRM, the samples were demagnetized in the AF field of 0, 5, 10, 15, 20, 30, 40, 50, 60, 80 and 100 mT, successively larger, and the remanences were measured after each demagnetization step. The measurements were made at the Institute of Astronomy and Geophysics of the University of São Paulo (IAG-USP) with a triaxial cryogenic magnetometer (2G, mod. 755).

ANHYSTERETIC REMANENT MAGNETIZATION (ARM)

ARM was acquired at a maximum AF field of 90 mT with a direct bias field of 50 μ T (hereafter referred to as ARM@90mT). The measurements were made at the IAG-USP with a triaxial cryogenic magnetometer (2G, mod. 755).

BACKFIELD ISOTHERMAL REMANENT MAGNETIZATION (BIRM)

BIRM experiments consisted of applying a strong magnetic field of 1 Tesla (T) and then applying a magnetic field of -0.1 and -0.3 T (in the opposite direction to the initial field), measuring the magnetization in the three steps. The measure provided the Saturation of Isothermal Remanent Magnetization (IRM@1T), BIRM@100mT and BIRM@300mT, respectively. The experiments were carried out on the triaxial cryogenic magnetometer at the IAG-USP and on the pulser. SIRM and BIRM-300mT were used to produce the S ratio@300mT, which is provided by -BIRM-300mT/SIRM (Liu et al., 2004). The S ratio reflects variations in the relative abundance of ferrimagnetic and antiferromagnetic minerals. When the S ratio is close to unity, low-coercivity minerals, such as magnetite and greigite, are interpreted to magnetically dominate samples. In contrast, when the S ratio is close to zero or has negative values, contributions from hematite and/or goethite are significant (Liu et al., 2004).

HYSTERESIS LOOPS

Hysteresis loops were carried out on seven samples powdered in an agate mortar. The samples were placed in gelatin capsules and the hysteresis loops were performed with a Princeton Measurements Corp. Model 3900 MicroMag™ Vibrating Sample Magnetometer (VSM) at the Centro Oceanográfico de Registros Estratigráficos (CORE) Laboratory of the Institute of Oceanography of the University of São Paulo (IO-USP).

The hysteresis loops and back-field remanence curves were used to determine magnetic saturation (Ms), magnetic saturation remanence (Mrs), coercivity (Hc) and remanence coercivity (Hcr). The Mrs/Ms and Hcr/Hc ratios were used as proxies for the magnetic domain state, in accordance with the Day diagram (Day et al., 1977). Grain size fields, single domain (SD), pseudo-single domain (PSD) and multi-domain (MD) were defined for the plots, for which lower Mrs/Ms values and higher Hcr/Hc values indicated multi-domain magnetic grains (Wasilewski, 1973; Day et al., 1977).

ISOTHERMAL REMANENT MAGNETIZATION (IRM)

The IRM acquisition experiments were carried out with the VSM in the CORE laboratory at IO-USP, subjecting the samples to increasing continuous magnetic fields of up to 1.2 T, applied at constant temperature over a timescale of a few seconds. The experimental protocol for IRM acquisition consists of measuring the remanent magnetization after each magnetic induction step up to the Saturation of IRM (SIRM). These measurements make it possible to characterize the spectrum of coercive force of the magnetic minerals present in the sediments and, consequently, to determine their relative contribution to the total IRM.

FIRST ORDER REVERSAL CURVE (FORC)

FORC experiments were carried out on seven powdered samples placed in gelatin capsules using the VSM of IO-USP. Each FORC diagram was calculated from a set of 259 partial hysteresis loop cycles (Mayergoyz, 1986). A FORC diagram is a contour plot of a FORC distribution in which H_u , on

the vertical axis, describes the switching field of the particle (i.e., coercivity) and H_c , on the horizontal axis, describes the local interaction field (Roberts et al., 2000). This experiment makes it possible to identify the contribution of superparamagnetic (SP), SD, PSD and MD grains to the magnetization of the sample (Roberts et al., 2000) and the presence or absence of magnetic interactions.

TEMPERATURE DEPENDENCE OF MAGNETIC SUSCEPTIBILITY

Thermomagnetic analyses were carried out on eight powdered samples in an argon atmosphere using the Multifunction MFK1 Kappabridge (AGICO) equipped with a CS-4 high-temperature furnace in the temperature range of 30–700 °C at the CORE Laboratory, IO-USP. The magnetic mineralogy was determined by estimating the Curie temperature and identifying mineralogical transformations during heating (e.g., Skinner et al., 1964; Krs et al., 1992; Dekkers et al., 2000; Roberts et al., 2011).

X-RAY FLUORESCENCE

XRF scanning measurements were made at 1 cm intervals directly on the surface of the split halfcore section using a third generation XRF-Scanning Avaatech at the Gulf Coast Repository of the International Ocean Discovery Program, at Texas A&M University. The XRF Scanning X-ray source was an Oxford Instruments 100 W Neptune X-ray tube with a rhodium (Rh) target, and data were collected using a Canberra X-PIPS silicon drift detector with 150 eV X-ray resolution at 5.9 keV and a Canberra Digital Spectrum Analyzer model DAS 1000. The surface of the half core at room temperature was covered with a 4 µm thick Ultralene plastic film to prevent contamination and desiccation of the sediment. Measurements were made at a resolution of 1 cm, with a beam size of 1 x 1 cm for two consecutive runs of the same section, the first one at 9 kV, 0.25 mA, and 6 s, and the second one at 30 kV, 1.25 mA, and 6 s.

The raw data of the elements of interest in each sample were normalized by dividing for the sum of all the elements detected in the respective

sample (element/sum). This procedure, which is called closure, eliminates the main problems related to the unprocessed sample (e.g., specimen inhomogeneity, variable water content and change in grain size) measured by the XRF scanning method (Kido et al., 2006; Tjallingii et al., 2007; Weltje and Tjallingii, 2008).

To improve confidence in the data collected with XRF scanning, discrete measurements on conventional XRF were performed on 42 samples collected at 3 cm intervals from the U1471C-1H-3W core section (3 to 4.5 mbsf). The samples, collected from 5 g aliquots the core material, were dried and powdered in an agate mortar. The powdered samples were measured in the conventional XRF Rigaku Supermini200 in the CORE laboratory at IO-USP. The correlation coefficient between the two methods was used to determine the reliability of the data from XRF scanning.

RESULTS AND DISCUSSION

THE LOSS OF REMANENCE AT THE TOP OF THE RECORD

The intensity of NRM@30mT obtained from 31 discrete samples and from BIRM experiments (BIRM@100mT, BIRM@300mT and IRM@1T) obtained from 11 U-channels are notably higher in the upper 2 mbsf than below this depth up to 15 mbsf (figure 2). The highest discrete sample measured, located at a depth of 0.06 mbsf, had an ARM@90mT value around 100 times greater than the other samples measured from two to 15 mbsf. The first suspicion is that this marked drop in remanence values may be related to contamination (e.g., rust contamination during drilling processes). We ruled out the contamination hypothesis based on XRF scanning data from the upper 15 mbsf, in which the Fe/sum curve showed a pattern that was not related to the marked drop in ARM@90mT values found in the upper two meters of the record (Figure 2). The reliability of the Fe/sum data from XRF scanning was guaranteed by a direct comparison with the conventional benchtop XRF carried out on the U1471C-1H-3W core

section ($r = 0.94431$). Thus, the drop in ARM@90mT values at the upper 2 mbsf is not related to changes

in the amount of iron-bearing minerals, but rather to changes in the oxidation state of Fe.

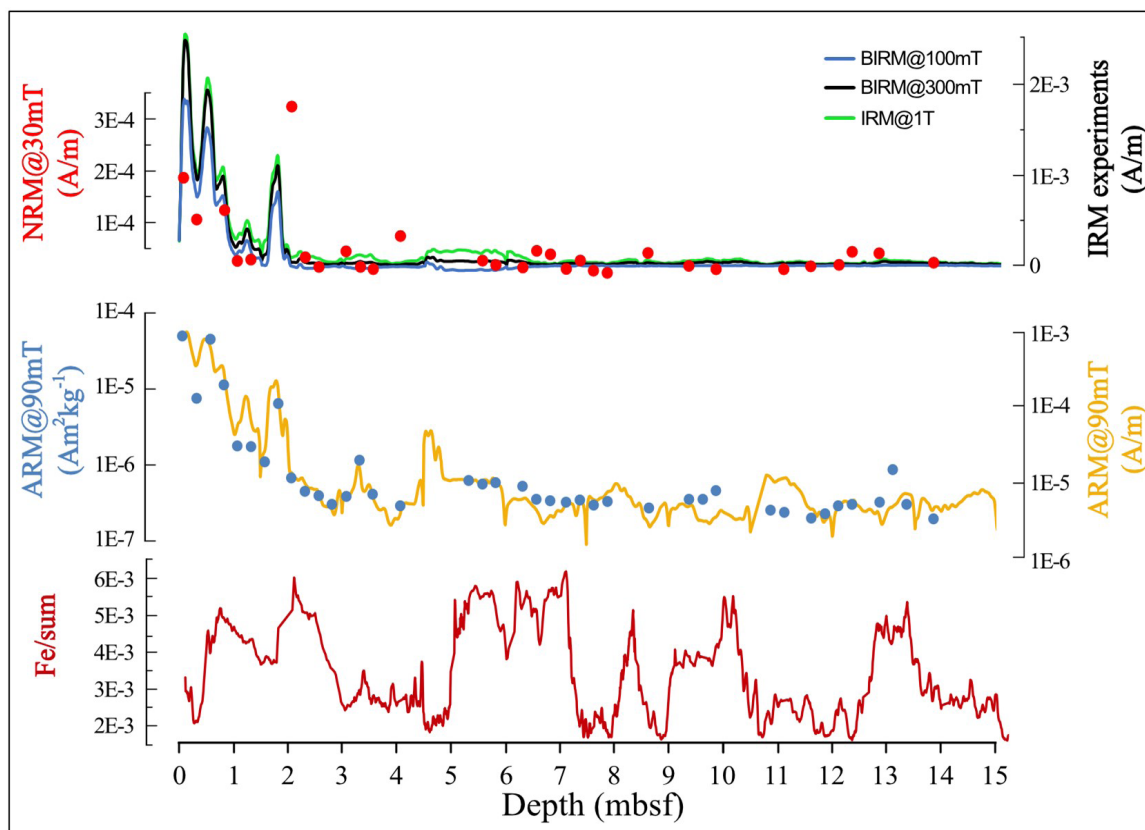


Figure 2. NRM@30mT intensity from 31 discrete samples compared with BIRM@100mT, BIRM@300mT and IRM@1T obtained at a resolution of 1 cm from U-channels in the upper 15 mbsf. The data show a drop in the remanence values at the top of the record. ARM@90mT data from 40 discrete samples and from U-channels compared with Fe/sum data obtained at a resolution of 1 cm with the XRF scanning method in the upper 15 mbsf. The data show a pattern for Fe/sum, different from the sharp drop in the upper 3 mbsf found for ARM@90mT.

THE DEGAUSSING OF NRM

The NRM demagnetization curves provided some information about the magnetic carriers. In the upper part of the record, at 0.06 mbsf (Figure 3; sample 1), soft minerals (which demagnetize in AF fields lower than 30 mT and represent the viscous component) dominate the NRM. In the two subsequent samples, at 0.31 and 0.56 mbsf (Figure 3; samples 2 and 3), the signal from soft minerals is reduced and the signal from harder minerals (which demagnetize in AF fields from 30 to 90 mT) is more representative. At 0.56 mbsf (Figure 3; sample 3), the increase in

remanence values in response to higher AF fields is due to the viscous component of NRM, which is in the opposite direction to the remanence acquired by harder minerals. Towards the lower part of the record, from 1.06 to 2.06 mbsf (Figure 3; samples 5-9), except for the record at 1.56 mbsf (Figure 3; sample 7), the contribution of harder minerals to NRM increases and reaches the maximum values in the interval studied. The sample at 1.56 mbsf does not demagnetize in AF fields lower than 90 mT. Below 2.31 mbsf (Figure 3; sample 10), the contribution of soft minerals to NRM increases, while the contribution of harder minerals is reduced.

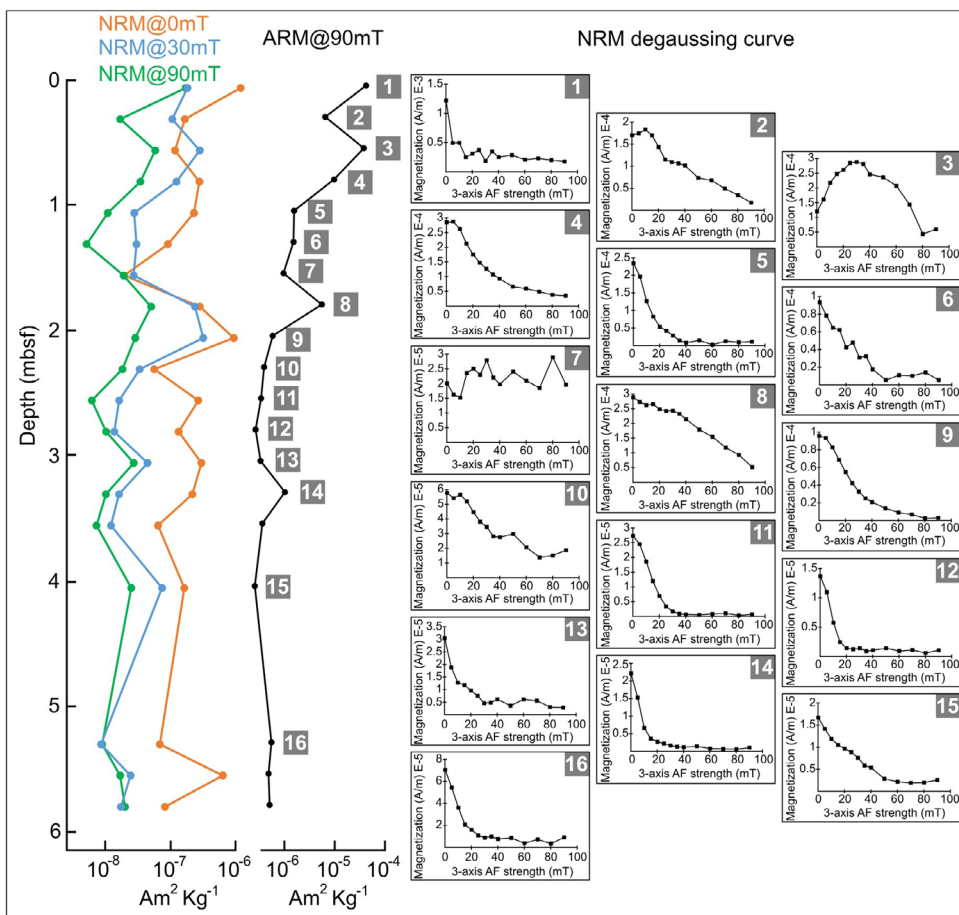


Figure 3. NRM time series at AF degaussing steps of 0 mT, 30 mT and 90 mT. ARM@90 mT is presented with the number of each sample selected to show the complete degaussing curves.

CHANGES IN MAGNETIC MINERALOGY AND GRAIN SIZE

In our record, the FORC diagrams at 0.06, 0.31, 0.56 and 0.81 mbsf (Figure 4; samples 1-4) show a signal close to $H_c = 0$ and spread along H_u , indicating the presence of low-coercivity PSD minerals (or a mixture of SD, PSD and MD) (Roberts et al., 2000). IRM acquisition saturates the samples in fields below 200 mT, supporting soft minerals (e.g., magnetite and greigite) as the main magnetic minerals present in this interval.

From 0.06 to 0.31 mbsf (Figure 4; from sample 1 to 2), the ARM@90mT values change from $4.53E-5$ ($\text{Am}^2\text{Kg}^{-1}$) to $7.03E-6$ ($\text{Am}^2\text{Kg}^{-1}$) as a result of the decrease in the concentration of soft minerals. The FORC diagrams show a more widespread signal in H_u , in response to the relative enrichment of MD grains

(Roberts et al., 2000). This result is in line with the Day diagram, which moves towards the MD region.

At 0.56 mbsf (Figure 4; sample 3), ARM@90mT shows high values again, $4.09E-5$ ($\text{Am}^2\text{Kg}^{-1}$), close to those found at 0.06 mbsf. The FORC diagrams show PSD contours, which corresponds to a greater influence of the SD component (Roberts et al., 2000). The day diagram corroborates the FORC results and moves towards the SD region.

From this point, the concentration of soft minerals decreases considerably. The ARM@90mT data drop to values close to $6.34E-7$ ($\text{Am}^2\text{Kg}^{-1}$) at 2.06 mbsf (Figure 4) and remain low until 15 mbsf (Figure 2). The IRM acquisition curves measured in samples with low ARM@90mT values at 1.06 and 2.56 mbsf (Figure 4; samples 5 and 7) show an increase in remanent magnetization in applied fields

from 200 mT to 1T. The remanence acquisition in these fields occurs due to the relative increase in

the concentration of minerals with higher coercivity (e.g., hematite).

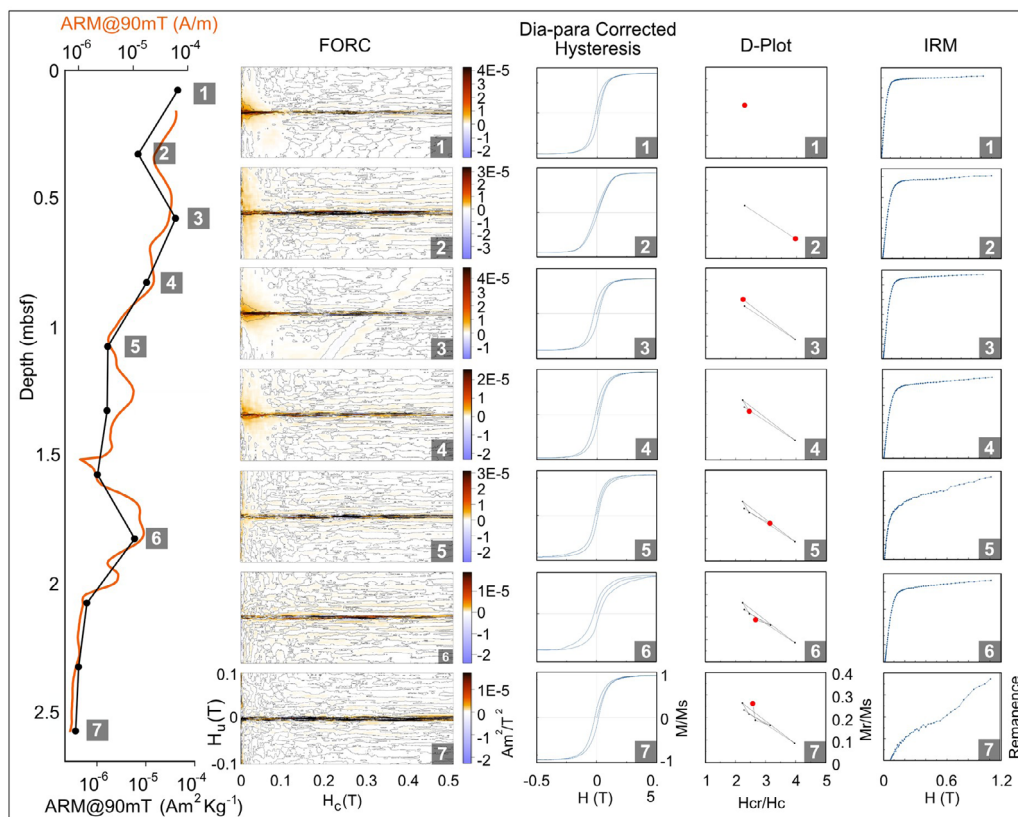


Figure 4. ARM@90mT corrected for mass (note that the data are plotted on a logarithmic scale). FORC diagrams measured with a mean time of 4 seconds per point. Dia-paramagnetic corrected hysteresis loop. Day diagram (red dots indicate the current sample) and acquisition of IRM.

TEMPERATURE-DEPENDENT MAGNETIC SUSCEPTIBILITY

High-temperature thermomagnetometry makes it possible to identify different magnetic minerals. Interpretations are made mainly using the characteristic Curie temperature of different minerals (e.g., magnetite and hematite), but also using well-documented chemical changes (Minyuk et al., 2011; Till and Nowaczyk, 2018; Muxworthy et al., 2023) during sample heating (e.g., greigite and siderite).

The thermomagnetic curves in samples at 0.06, 0.56, 0.81, 1.81 and 2.56 mbsf (Figure 5; samples A, C-F) show similar behavior, with low susceptibility values before the samples reach temperatures of around 450°C. Continuing to heat the samples, the susceptibility increases and reaches maximum values at 520°C, from

where it drops, returning to values close to zero at 580°C. After heating to 700°C, the cooling curves towards room temperature show higher susceptibility values, which indicates the occurrence of chemical transformations during sample heating. We attribute these results to the presence of siderite (FeCO_3) in the samples.

Siderite is paramagnetic at room temperature and has a low susceptibility, but during heating (at temperatures around 400–500°C), susceptibility increases as siderite progressively converts to magnetite (Housen et al., 1996; Abdulkarim et al., 2022; Muxworthy et al., 2023). The formation of magnetite during the heating of siderite is evidenced by the Curie temperature of 580°C, at which the sample demagnetizes (Figure 5; samples A, C-F). Thermomagnetic curves also show that, at room

temperature, the product of sample heating has a higher susceptibility than the unheated samples, which is in line with the formation of magnetite from siderite during heating (Housen et al., 1996; Abdulkarim et al., 2022; Muxworthy et al., 2023).

Despite the common presence of siderite, the thermomagnetic curves of the samples at 0.06 and 0.56 mbsf (Figure 5; A and C) differ slightly from those of the samples at 0.81, 1.81 and 2.56 mbsf (Figure 5; samples D-F) and show a susceptibility at room temperature higher than the susceptibility found at temperatures above the Curie temperature.

This result indicates that a magnetic mineral is present in these two samples. The heating curves of these samples show a single Curie temperature at 580°C, at which the entire sample is demagnetized, and although most of the signal is related to the magnetite formed by heating the siderite, the mineral in question should demagnetize at the same temperature. We interpret this mineral as magnetite due to its Curie temperature of 580°C. These results indicate that magnetite is the main magnetic carrier (Housen et al., 1996) currently sedimenting at the site.

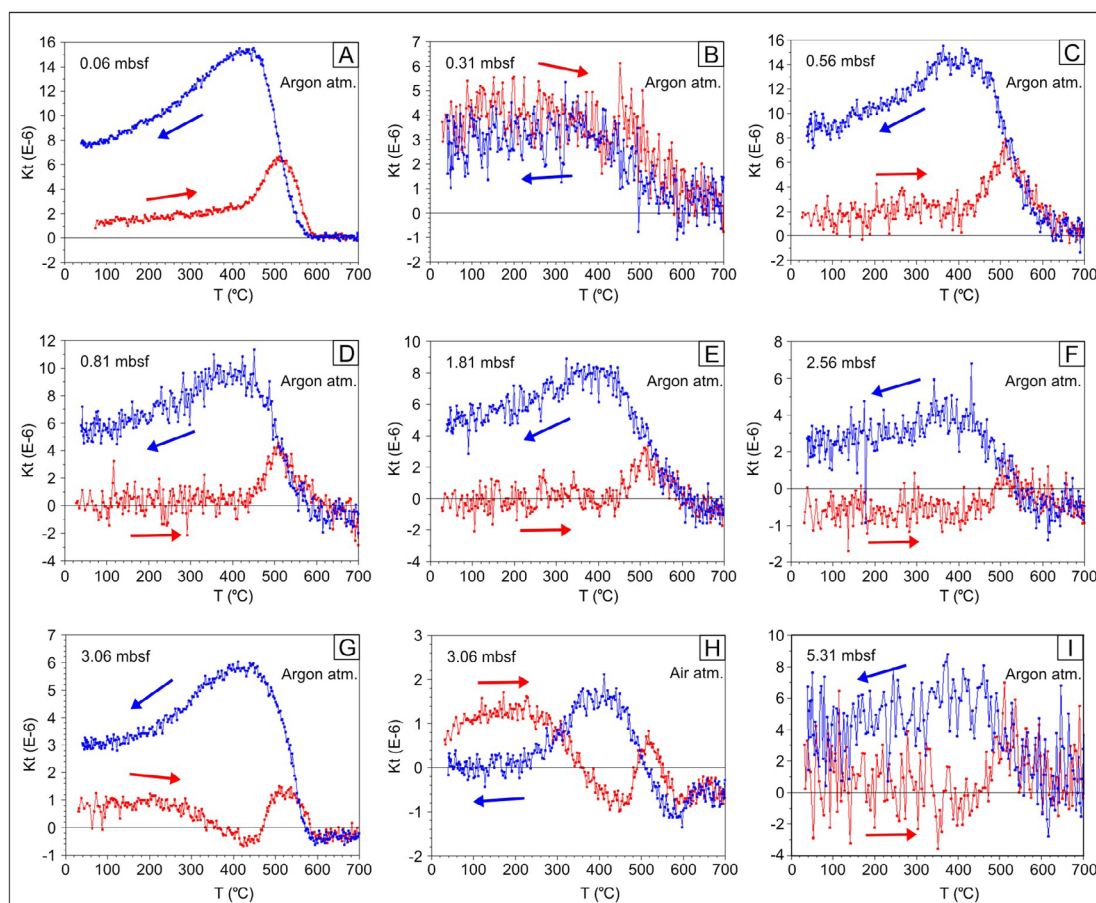


Figure 5. Temperature-dependent magnetic susceptibility corrected for the diamagnetic contribution of the furnace. The heating and cooling curves are plotted in red and blue, respectively.

At 3.06 mbsf (Figure 5; sample G), the magnetic mineralogy changes and, starting from room temperature, the thermomagnetic heating curve shows an increase in susceptibility until it reaches a peak at a temperature of around 250°C. As the sample continues to heat up, the susceptibility starts

to decrease and reaches a minimum at a temperature of around 440°C. Increasing the temperature further, the susceptibility increases again, reaching a second peak at a temperature of around 520°C and then decreases again, becoming demagnetized at a temperature of around 580°C.

We associate these results to the thermomagnetic behavior of greigite. During heating, greigite shows a Hopkinson peak from 240°C to 250°C (Muxworthy et al., 2023), followed by a sharp decrease in susceptibility at ~400°C associated with its chemical transformation into sulphur, pyrite, marcasite and pyrrhotite (Skinner et al., 1964; Krs et al., 1992; Torii et al., 1996; Muxworthy et al., 2023;), which leads to a decrease in magnetization (Dekkers et al., 2000). Heating greigite from 450°C to 550°C in an argon atmosphere forms pyrrhotite, while heating it to 550°C, 650°C and 700°C leads to the progressive formation of magnetite. Heating greigite under conditions of increased oxygen availability produces hematite (Fe₂O₃) (Dekkers et al., 2000; Roberts et al., 2011). To confirm the presence of greigite in this sample, a second aliquot was measured, but this time in an air atmosphere. The heating curve of this aliquot (Figure 5; sample H) differs from that of the aliquot measured under argon atmosphere (Figure 5; sample G), and the susceptibility starts to increase at temperatures higher than 580°C, reaching a peak at a temperature of around 660°C. This difference is associated with the Hopkinson peak of hematite and is explained by the greater amount of hematite formed due to the greater availability of oxygen during the heating of the sample. The product of the heated sample also shows this difference and the susceptibility, at room temperatures, is lower in the sample that was heated in an air atmosphere compared to the sample that was heated in an argon atmosphere, possibly due to the smaller amount of magnetite that was formed during heating.

At 5.56 mbsf (Figure 5; sample I), the thermomagnetic curves are very noisy, but it is still possible to identify a behavior similar to that found for the sample at 3.06 mbsf (Figure 5; sample G), which indicates the presence of greigite.

THE EVIDENCE OF MAGNETITE REDUCTION AND GREIGITE GROWTH

The detrital sediments in the Inner Sea of the Maldives are mainly of aeolian origin from the deserts of the Indian-Asian landmass. Their variation over time is related to the expansion and retraction of the arid zones with a ~100 kyr cyclicity and to the intensity of the Indian winter monsoon winds with a ~20 kyr

cyclicity (Kunkelova et al., 2018; Carrasqueira et al., 2023). Therefore, as it was related to the Fe/sum record, the variation in magnetic parameters related to material provenance should show this cyclicity. The magnetic parameters have no correlation with the Fe/sum record (Figure 6), therefore, changes such as the sharp drop in remanence values at the top of the record, followed by the S ratio (Figure 6; arrow 1), the small increase in remanence values at 3 mbsf (Figure 6; arrow 2) and the increase in the S ratio at 6 to 7 mbsf (Figure 6; arrow 5) cannot be explained by changes in the provenance of the material and must be related to geochemical changes in the sediment.

Magnetite reduction under sulfidic conditions is a common diagenetic process. Widely reported in marine sediments, it is characterized by a marked loss of remanence in the upper few meters of the sedimentary column (Liu et al., 2004; Rowan and Roberts, 2006; Rowan et al., 2009; Rodelli et al., 2019, 2018), exactly as found in our record (Figure. 2).

During the sulfidic dissolution of magnetite (Rowan and Roberts, 2006; Rowan et al., 2009), the fine fraction is preferentially reduced in relation to the coarser, which, due to its higher surface area to volume ratio (Rowan and Roberts, 2006; Rowan et al., 2009; Rodelli et al., 2019), leads to a relative enrichment of MD magnetite. In our record, the processes resemble the transition found in the interval from 0.06 to 0.31 m (Figure 4; samples 1 to 2). We interpret this interval as the modern sulfidic dissolution front, located just below the water-sediment interface.

In many records, a secondary peak in remanence values just below the sulfidic dissolution front has been associated with the old dissolution front (Rowan et al., 2009). A recent upward migration of the old sulfidic dissolution front in the sedimentary column left an interval with incomplete magnetite reduction. This migration has been associated with the environmental changes of the early Holocene, which altered sediment grain size and porewater geochemistry (Rowan et al., 2009). In our record, a secondary peak in remanence values was found at 0.56 mbsf (Figure 4; sample 3). According to the most recently published chronology for record U1471 (Carrasqueira et al., 2023), this sample is

13.1 Ka old (just before the start of the Holocene). In the sedimentary records of the Inner Sea of the Maldives, the Holocene was characterized by increased mud deposition, leading to a decrease in

porosity (Paul et al., 2012; Lindhorst et al., 2019). The combined effect of the modern and old dissolution front resulted in a huge decrease in remanence values from zero to 2 mbsf (Figure 6; arrow 1).

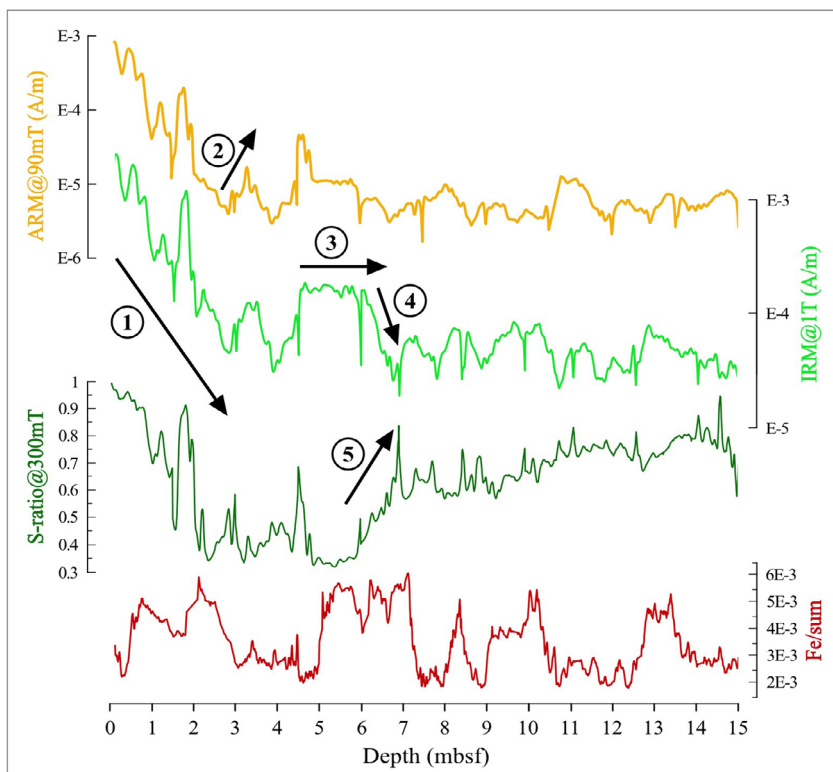


Figure 6. ARM@90mT, IRM@1T, S ratio@300mT and Fe/sum data obtained at a resolution of 1 cm from U-channels and half cores in the upper 15 mbsf.

It has previously been reported that, in sulfidic environments, hematite can persist for longer periods than magnetite (Robinson et al., 2000; Yamazaki et al., 2003; Emirođlu et al., 2004; Liu et al., 2004; Poulton et al., 2004; Garming et al., 2005; Rey et al., 2005; Kawamura et al., 2007; Rowan et al., 2009; Roberts, 2015;). In our record, the drop in remanence values from 0 to 2 mbsf (Figure 6; arrow 1) is associated with a relative increase in the contribution of hard minerals (e.g., hematite), as suggested by the S ratio obtained from the U-channels, which shows an increasing trend, going from values close to one at the top of the record to values close to 0.4 at around 2 mbsf (Figure 6; arrow 1). The acquisition of remanence in fields higher than 200 mT in the samples at 1.06 and 2.56 mbsf (Figure 4; samples 5 and 7) confirm

this increase in the relative contribution of hard minerals.

Below the sulfidic dissolution front, the released iron reacts with H₂S to form a series of minerals, including greigite (Fe₃S₄) (Roberts and Weaver, 2005; Rowan and Roberts, 2006; Roberts et al., 2011). The authigenic growth of greigite starts from small SP particles, which do not carry remanence until they grow large enough to cross the stable size limit of SD (Rowan and Roberts, 2006; Rowan et al., 2009). In our record, greigite is clearly present in the thermomagnetic curves of the sample at 3.06 mbsf (Figure 5; samples G and H). The appearance of the greigite signal in a record just below magnetite dissolution raises a question: is the magnetite signal masking the greigite signal and, therefore, was the greigite

already present in the sample at the time of sedimentation or did it form authigenically? Considering that the magnetite is masking the greigite implies that, in the sample in which we found the greigite signal, the magnetite was preferentially reduced before the greigite became pyrite. If the greigite was there before and if its signal was masked by the presence of magnetite, we would expect the greigite signal to become more evident at some point along the dissolution front, where the magnetite would be reduced before the greigite became pyrite, possibly in the same samples in which the relative concentration of hard minerals increased in response to magnetite reduction (Figure 4; samples 5 and 7). Our thermomagnetic data, in contrast, show the greigite signal more than a meter below the point from where the sedimentary record lost almost all remanence, and we therefore discarded the detrital greigite hypothesis. To better support the hypothesis of authigenic greigite growth, we examined the interval just above (Figure 7; interval A) the sample where we found the greigite signal (figure 7; interval B). In interval A, the Fe/sum ratio is high compared to that in interval B, indicating a greater input of lithogenic minerals; on the other hand, lower ARM@90mT and IRM@1T values suggest lower concentrations of magnetite and greigite. From interval A to B (Figure 7), the increase in the concentration of soft minerals (ARM@90mT), identified as greigite in the thermomagnetic analysis, combined with the decrease in the lithogenic contribution, leads us to suggest that the greigite grew authigenically.

The authigenic growth of greigite records the geomagnetic field at a different period to that of sediment deposition. If authigenic greigite is currently crossing the SD stable grain size barrier in this depth interval, the modern geomagnetic field is currently being recorded in the sediment at these depths. According to the recently published chronology for Site U1471 (Carrasqueira et al., 2023), at 2.8 and 3.3 mbsf the record has ages of 102 and 103 Ka, respectively, so there is a possibility that the magnetostratigraphy-based chronology for Site U1471 has an error of almost

100 Ka. Below this depth, the ARM@90 mT data vary, but remain around an average, and peaks similar to the values found at 3.2 mbsf are also seen at depths of 4.6, 8 and 11 mbsf.

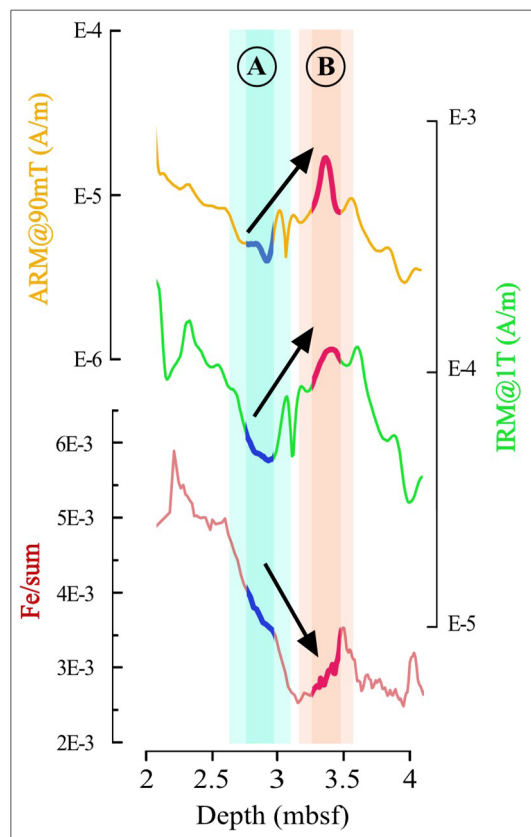


Figure 7. Comparison between continuous ARM@90mT, IRM@1T and Fe/sum data for the interval between 2 and 4 mbsf. Arrows indicate changes in the mean values between intervals A and B.

The IRM@1T data reach a plateau from 4 to 6 mbsf (Figure 6; arrow 3). These results are directly related to a higher concentration of hard minerals, as indicated by the low S ratio values (Figure 6). We associate this plateau with a greater supply of terrigenous sediments to the Maldives, as suggested by the high values of the Fe/sum ratio (Figure 6). From 6 to 7 mbsf, all remanence values decrease, and the drop in IRM@1T values (Figure 6; arrow 4) seems particularly more accentuated than the drop in ARM@90mT values. The large reduction in the contribution of hard minerals during this interval is indicated by the increase in S ratio values from

0.35 at a depth of 6 mbsf to 0.65 at a depth of 7 mbsf (Figure 6; arrow 5). These results suggest that, at these depths, the hard minerals are finally dissolved.

Below 7 mbsf, the S ratio values continue their upward trend with a lower gradient and reach values of around 0.8 at a depth of 14 mbsf (Figure 6). This result suggests that soft minerals persist in the record and that pyritization is incomplete in the studied interval. The preservation of soft minerals has been reported in a sedimentary record from the Inner Sea of the Maldives for the interval from 3 to 5 Ma (Lanci et al., 2019), and although the author reported many problems with the NRM data, it was still possible to establish a magnetostratigraphy-based chronology with reasonable reliability.

THE EFFECT OF DIFFUSION AND ADVECTION ON SP PARTICLES

At Site U1471, the upper 10 mbsf are affected by currents that cause the advection of bottom waters through the upper portion of the sediments (Kramer et al., 2000; Swart, 2000; Moore and Swart, 2022). The almost complete dissolution of magnetite in the upper 2 mbsf and the subsequent growth of greigite from an SP size to an SD size with a measurable signal, as found at 3.06 mbsf, indicates that at some point between these two events Fe^{2+} was available to be transported by diffusion and/or advection of the interstitial water and recrystallize in a different stratum. This process may have compromised the reliability of the Fe record, which is currently used to address changing arid conditions in the Indian-Asian landmass (e.g., Kunkelova et al., 2018; Carrasqueira et al., 2023).

To check whether the Fe record was compromised by the vertical movement of Fe^{2+} in the sedimentary column during magnetite reduction, we compared the Fe/sum record with the Si/sum and K/sum records. The Fe, Si and K present in the sediments of the Inner Sea of the Maldives have previously been associated with the delivery of detrital material and should therefore have a high correlation with each other (Kunkelova et al., 2018; Carrasqueira et al., 2023). The different minerals containing these elements respond differently to reducing conditions, thus, if the vertical movement of Fe^{2+} in the sediment is significant, then the Fe,

Si and K records must be displaced, showing low correlations or being out of phase.

To check for significant relative movement between these elements, we used data from the XRF scanning. The reliability of the XRF scanning data is guaranteed by their correlation with conventional benchtop XRF data (Fe: $r = 0.94$; Si: $r = 0.86$; and K: $r = 0.89$; Carrasqueira et al., 2023). The cross-correlation between the Fe/sum, Si/sum and K/sum obtained with the XRF scan shows maximum correlations without lag (Fe/sum vs. Si/sum lagged by 2 cm and Fe/sum vs. K/sum in phase; Figure 8), indicating that there is no significant relative movement between these elements after sedimentation and therefore suggesting that they preserve their depositional characteristics and can be used reliably.

Although the Fe/sum record preserves its depositional characteristics, we have no information on what percentage of Fe in the sediment is associated with magnetite. Thus, if this percentage is very low, a large vertical movement of the iron-rich SP particles would not be able to significantly alter the Fe content that was deposited in each layer.

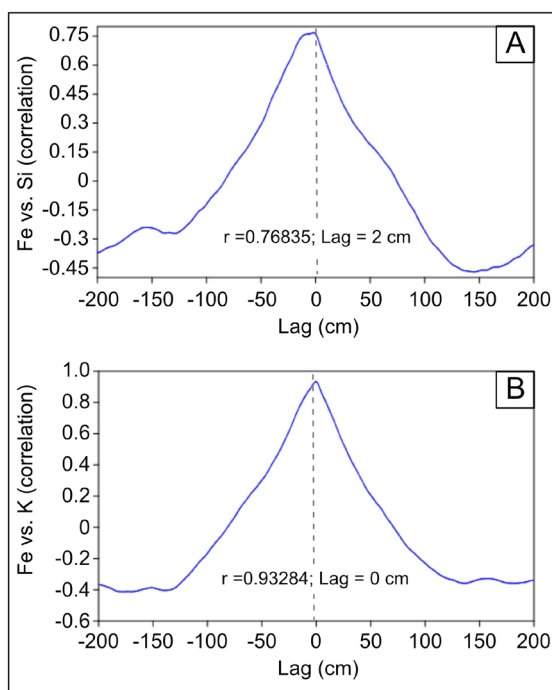


Figure 8. Cross-correlation between the records (A) Fe/sum vs. Si/sum and (B) Fe/sum vs. K/sum. The dashed vertical line shows the point of maximum correlation.

CONCLUSION

In the U1471 record, the reduction of magnetite shortly after the deposition of the sediment and the subsequent growth of greigite destroyed the primary NRM, imprinting a secondary NRM. Although the site has a restricted lithogenic fraction with limited reactive iron, the data suggest that there is no complete pyritization, and a geomagnetic chronology could be obtained from the greigite record. The secondary NRM recorded by greigite growth after magnetite reduction may currently be delayed by about 100 kyr in relation to the time of sediment deposition. Although the greigite record incorporates a delay in the magnetostratigraphy-based chronology, it may still represent an improvement in the chronology based on biostratigraphy, which currently has a discrepancy of around 500 kyr between the records of nannofossils and planktonic foraminifera.

ACKNOWLEDGMENTS

We would like to thank the crew of JOIDES Resolution for their assistance during core collection, the Centro Oceanográfico de Registros Estratigráficos (CORE), the Laboratório de Paleomagnetismo e Magnetismo de Rochas (USPMag) of the University of São Paulo and the IODP at Texas A&M for their support in data acquisition. We would also like to thank the reviewers for their comments that helped improve this work. This study was funded in part by the Coordenação de Aperfeiçoamento de Pessoal de Nível Superior - Brasil (CAPES) - Finance Code 001, L.J. and the CORE lab are supported by the Fundação de Amparo à Pesquisa do Estado de São Paulo (FAPESP) grant 2016/24946-9.

AUTHOR CONTRIBUTIONS

I.G.F.C.: Conceptualization; Formal Analysis; Investigation; Methodology; Visualization; Writing – Original draft; Writing – Review & editing.

L.L.: Conceptualization; Methodology; Resources; Supervision; Writing – Review & editing.

L.J.: Conceptualization; Funding acquisition; Methodology; Project administration; Resources; Supervision; Writing – Review & editing.

REFERENCES

Abdulkarim, M. A., Muxworthy, A. R., Fraser, A., Neumaier, M., Hu, P. & Cowan, A. 2022. Siderite

occurrence in petroleum systems and its potential as a hydrocarbon-migration proxy: A case study of the Catcher Area Development and the Bittern area, UK North Sea. *Journal of Petroleum Science and Engineering*, 212, 110248. DOI: <https://doi.org/10.1016/j.petrol.2022.110248>

Berner, R. A. 1984. Sedimentary pyrite formation: An update. *Geochimica et Cosmochimica Acta*, 48, 605–615. DOI: [https://doi.org/10.1016/0016-7037\(84\)90089-9](https://doi.org/10.1016/0016-7037(84)90089-9)

Betzler, C., Eberli, G. P., Alvarez Zarikian, C. A., Alonso-García, M., Bialik, O. M., Blättler, C. L., Guo, J. A., Haffen, S., Horozal, S., Inoue, M., Jovane, L., Kroon, D., Lanci, L., Laya, J. C., Ling Hui Mee, A., Lüdmann, T., Nakakuni, M., Nath, B. N., Niino, K., Petruny, L. M., Pratiwi, S. D., Reijmer, J. J. G., Reolid, J., Slagle, A. L., Sloss, C. R., Su, X., Swart, P. K., Wright, J. D., Yao, Z. & Young, J. R. 2017a. Site U1471. In: Betzler, C., Eberli, G. P., Alvarez Zarikian, C. A. & The Expedition 359 Scientists. *Maldives Monsoon and Sea Level. Proceedings of the International Ocean Discovery Program*. College Station, TX (International Ocean Discovery Program). DOI: <http://dx.doi.org/10.14379/iodp.proc.359.109.2017>

Betzler, C., Eberli, G. P., Alvarez Zarikian, C. A., Alonso-García, M., Bialik, O. M., Blättler, C. L., Guo, J. A., Haffen, S., Horozal, S., Inoue, M., Jovane, L., Kroon, D., Lanci, L., Laya, J. C., Ling Hui Mee, A., Lüdmann, T., Nakakuni, M., Nath, B. N., Niino, K., Petruny, L. M., Pratiwi, S. D., Reijmer, J. J. G., Reolid, J., Slagle, A. L., Sloss, C. R., Su, X., Swart, P. K., Wright, J. D., Yao, Z. & Young, J. R. 2017b. Site U1468. In Betzler, C., Eberli, G.P., Alvarez Zarikian, C.A. & The Expedition 359 Scientists. *Maldives Monsoon and Sea Level. Proceedings of the International Ocean Discovery Program*. College Station, TX (International Ocean Discovery Program). DOI: <http://dx.doi.org/10.14379/iodp.proc.359.106.2017>

Betzler, C., Eberli, G. P., Lüdmann, T., Reolid, J., Kroon, D., Reijmer, J. J. G., Swart, P. K., Wright, J., Young, J. R., Alvarez-Zarikian, C., Alonso-García, M., Bialik, O. M., Blättler, C. L., Guo, J. A., Haffen, S., Horozal, S., Inoue, M., Jovane, L., Lanci, L., Laya, J. C., Hui Mee, A. L., Nakakuni, M., Nath, B.N., Niino, K., Petruny, L. M., Pratiwi, S. D., Slagle, A. L., Sloss, C. R., Su, X. & Yao, Z. 2018. Refinement of Miocene sea level and monsoon events from the sedimentary archive of the Maldives (Indian Ocean). *Progress in Earth and Planetary Science*, 5, 5. DOI: <https://doi.org/10.1186/s40645-018-0165-x>

Betzler, C., Eberli, G., Kroon, D., Wright, J., Swart, P., Bejugam, N., Zarikian, C., Alonso Garcia, M., Bialik, O., Blättler, C., Guo, J., Haffen, S., Horozal, S., Inoue, M., Jovane, L., Lanci, L., Laya, J.C., Ling, A., Lüdmann, T. & Young, J. 2016. The abrupt onset of the modern South Asian Monsoon winds. *Scientific Reports*, 6. DOI: <https://doi.org/10.1038/srep29838>

Betzler, C., Fürstenau, J., Lüdmann, T., Hübscher, C., Lindhorst, S., Paul, A., Reijmer, J. J. G. & Droxler, A. W. 2013a. Sea-level and ocean-current control on carbonate-platform growth, Maldives, Indian Ocean. *Basin Research*, 25, 172–196. DOI: <https://doi.org/10.1111/j.1365-2117.2012.00554.x>

Betzler, C., Hübscher, C., Lindhorst, S., Reijmer, J. J. G., Römer, M., Droxler, A. W., Fürstenau, J. & Lüdmann,

- T. 2009. Monsoon-induced partial carbonate platform drowning (Maldives, Indian Ocean). *Geology*, 37(10), 867–870. DOI: <https://doi.org/10.1130/G25702A.1>
- Betzler, C., Lüdmann, T., Hübscher, C. & Fürstenau, J. 2013b. Current and sea-level signals in periplatform ooze (Neogene, Maldives, Indian Ocean). *Sedimentary Geology*, 290, 126–137. DOI: <https://doi.org/10.1016/j.sedgeo.2013.03.011>
- Bunzel, D., Schmiedl, G., Lindhorst, S., Mackensen, A., Reolid, J., Romahn, S. & Betzler, C. 2017. A multi-proxy analysis of Late Quaternary ocean and climate variability for the Maldives, Inner Sea. *Climate of the Past*, 13, 1791–1813. DOI: <https://doi.org/10.5194/cp-13-1791-2017>
- Carrasqueira, I. G. F., Jovane, L., Droxler, A. W., Alvarez Zirikian, C. A., Lanci, L., Alonso-García, M., Laya, J. C. & Kroon, D. 2023. Anomalous widespread arid events in Asia over the past 550,000 years. *PNAS Nexus*, 2(6). DOI: <https://doi.org/10.1093/pnasnexus/pgad175>
- Dantas, R. C., Hassan, M. B., Cruz, F. W. & Jovane, L. 2022. Evidence for methane seepage in South Atlantic from the occurrence of authigenic gypsum and framboidal pyrite in deep-sea sediments. *Marine and Petroleum Geology*, 142, 105727. DOI: <https://doi.org/10.1016/j.marpetgeo.2022.105727>
- Day, R., Fuller, M. & Schmidt, V. A. 1977. Hysteresis properties of titanomagnetites: Grain-size and compositional dependence. *Physics of the Earth and Planetary Interiors*, 13, 260–267. DOI: [https://doi.org/10.1016/0031-9201\(77\)90108-X](https://doi.org/10.1016/0031-9201(77)90108-X)
- Dekkers, M. J., Passier, H. F. & Schoonen, M. A. A. 2000. Magnetic properties of hydrothermally synthesized greigite (Fe₃S₄)—II. High- and low-temperature characteristics. *Geophysical Journal International*, 141, 809–819. DOI: <https://doi.org/10.1046/j.1365-246x.2000.00129.x>
- Droxler, A. W., Haddad, D. A., Mucciarone, J. L. & Cullen, J. L. 1990. Pliocene-Pleistocene Aragonite Cyclic Variations in Holes 714A and 716B (the Maldives) Compared with Hole 633A (the Bahamas): Records of Climate-Induced CaCO₃ Preservation at Intermediate Water Depths. *Proceedings of the Ocean Drilling Program, Scientific Result*, 115. DOI: <https://doi.org/10.2973/odp.proc.sr.115.179.1990>
- Emiroğlu, S., Rey, D. & Petersen, N. 2004. Magnetic properties of sediment in the Ría de Arousa (Spain): dissolution of iron oxides and formation of iron sulphides. *Physics and Chemistry of the Earth, Parts A/B/C*, 29, 947–959. DOI: <https://doi.org/10.1016/j.pce.2004.03.012>
- Florindo, F. & Sagnotti, L. 1995. Palaeomagnetism and rock magnetism in the upper Pliocene Valle Ricca (Rome, Italy) section. *Geophysical Journal International*, 123(2), 340–354. DOI: <https://doi.org/10.1111/j.1365-246X.1995.tb06858.x>
- Garming, J. F. L., Bleil, U. & Riedinger, N. 2005. Alteration of magnetic mineralogy at the sulfate–methane transition: Analysis of sediments from the Argentine continental slope. *Physics of the Earth and Planetary Interiors*, 151, 290–308. DOI: <https://doi.org/10.1016/j.pepi.2005.04.001>
- Housen, B. A., Banerjee, S. K. & Moskowitz, B. M. 1996. Low-temperature magnetic properties of siderite and magnetite in marine sediments. *Geophysical Research Letters*, 23, 2843–2846. DOI: <https://doi.org/10.1029/96GL01197>
- Jiang, W.-T., Horng, C.-S., Roberts, A. P. & Peacor, D. R. 2001. Contradictory magnetic polarities in sediments and variable timing of neof ormation of authigenic greigite. *Earth and Planetary Science Letters*, 193(1-2), 1–12. DOI: [https://doi.org/10.1016/S0012-821X\(01\)00497-6](https://doi.org/10.1016/S0012-821X(01)00497-6)
- Kao, S.-J., Horng, C.-S., Roberts, A. P. & Liu, K.-K. 2004. Carbon–sulfur–iron relationships in sedimentary rocks from southwestern Taiwan: influence of geochemical environment on greigite and pyrrhotite formation. *Chemical Geology*, 203(1-2), 153–168. DOI: <https://doi.org/10.1016/j.chemgeo.2003.09.007>
- Kawamura, N., Oda, H., Ikehara, K., Yamazaki, T., Shioi, K., Taga, S., Hatakeyama, S. & Torii, M. 2007. Diagenetic effect on magnetic properties of marine core sediments from the southern Okhotsk Sea. *Earth, Planets and Space*, 59, 83–93. DOI: <https://doi.org/10.1186/BF03352680>
- Kido, Y., Koshikawa, T. & Tada, R. 2006. Rapid and quantitative major element analysis method for wet fine-grained sediments using an XRF microscanner. *Marine Geology*, 229, 209–225. DOI: <https://doi.org/10.1016/j.margeo.2006.03.002>
- Kramer, P., Swart, P., De Carlo, E. H. & Schovsbo, N. H. 2000. Overview of interstitial fluid and sediment geochemistry, Sites 1003–1007 (Bahamas Transect). *Proceedings of the Ocean Drilling Program, Scientific Results*, 166, 1003–1007. DOI: <https://doi.org/10.2973/odp.proc.sr.166.117.2000>
- Krs, M., Novák, F., Krsová, M., Pruner, P., Kouklíková, L. & Jansa, J. 1992. Magnetic properties and metastability of greigite-smythite mineralization in brown-coal basins of the Krušné hory Piedmont, Bohemia. *Physics of the Earth and Planetary Interiors*, 70, 273–287. DOI: [https://doi.org/10.1016/0031-9201\(92\)90194-Z](https://doi.org/10.1016/0031-9201(92)90194-Z)
- Kunkelova, T., Jung, S.J.A., De Leau, E. S., Odling, N., Thomas, A. L., Betzler, C., Eberli, G.P., Alvarez-Zarikian, C. A., Alonso-García, M., Bialik, O. M., Blättler, C. L., Guo, J. A., Haffen, S., Horozal, S., Mee, A. L. H., Inoue, M., Jovane, L., Lanci, L., Laya, J. C., Lüdmann, T., Bejugam, N. N., Nakakuni, M., Niino, K., Petruny, L. M., Pratiwi, S. D., Reijmer, J. J. G., Reolid, J., Slagle, A. L., Sloss, C. R., Su, X., Swart, P. K., Wright, J. D., Yao, Z., Young, J. R., Lindhorst, S., Stainbank, S., Rueggeberg, A., Spezzaferri, S., Carrasqueira, I., Yu, S. & Kroon, D. 2018. A two million year record of low-latitude aridity linked to continental weathering from the Maldives. *Progress in Earth and Planetary Science*, 5, 86. DOI: <https://doi.org/10.1186/s40645-018-0238-x>
- Lanci, L., Zanella, E., Jovane, L., Galeotti, S., Alonso-García, M., Alvarez-Zarikian, C. A., Bejugam, N. N., Betzler, C., Bialik, O. M., Blättler, C. L., Eberli, G. P., Guo, J. A., Haffen, S., Horozal, S., Inoue, M., Kroon, D., Laya, J. C., Mee, A. L. H., Lüdmann, T., Nakakuni,

- M., Niino, K., Petruny, L. M., Pratiwi, S. D., Reijmer, J. J. G., Reolid, J., Slagle, A. L., Sloss, C. R., Su, X., Swart, P. K., Wright, J. D., Yao, Z. & Young, J. R. 2019. Magnetic properties of early Pliocene sediments from IODP Site U1467 (Maldives platform) reveal changes in the monsoon system. *Palaeogeography, Palaeoclimatology, Palaeoecology*, 533, 109283. DOI: <https://doi.org/10.1016/j.palaeo.2019.109283>
- Lindhorst, S., Betzler, C. & Kroon, D. 2019. Wind variability over the northern Indian Ocean during the past 4 million years – insights from coarse aeolian dust (IODP Exp. 359, Site U1467, Maldives). *Palaeogeography, Palaeoclimatology, Palaeoecology*, 536, 109371. DOI: <https://doi.org/10.1016/j.palaeo.2019.109371>
- Liu, J., Zhu, R., Roberts, A. P., Li, S. & Chang, J.-H. 2004. High-resolution analysis of early diagenetic effects on magnetic minerals in post-middle-Holocene continental shelf sediments from the Korea Strait. *Journal of Geophysical Research Solid Earth*, 109. DOI: <https://doi.org/10.1029/2003JB002813>
- Malone, M., Baker, P.A., Burns, S. & Swart, P. 1990. 35. Geochemistry of Periplatform Carbonate Sediments, Leg 115, Site 716 (Maldives Archipelago, Indian Ocean). *Proceedings of the Ocean Drilling Program, Scientific Result*, 115.
- Mayergoyz, I. 1986. Mathematical Models of Hysteresis. *IEEE Transactions on Magnetics*, 22(5), 603–608. <https://doi.org/10.1109/TMAG.1986.1064347>
- Minyuk, P. S., Subbotnikova, T. V. & Plyashkevich, A. A. 2011. Measurements of thermal magnetic susceptibility of hematite and goethite. *Izvestiya, Physics of the Solid Earth*, 47, 762–774. DOI: <https://doi.org/10.1134/S1069351311080052>
- Moore, E. W. & Swart, P. K. 2022. Evidence for recrystallization and fluid advection in the Maldives using the sulfur isotopic composition of porewaters, carbonates, and celestine. *Chemical Geology*, 609, 121062. DOI: <https://doi.org/10.1016/j.chemgeo.2022.121062>
- Muxworthy, A. R., Turney, J. N., Qi, L., Baker, E. B., Perkins, J. R. & Abdulkarim, M. A. 2023. Interpreting high-temperature magnetic susceptibility data of natural systems. *Frontiers in Earth Science*, 11. DOI: <https://doi.org/10.3389/feart.2023.1171200>
- Ogg, J. G. 2020. Chapter 5 - Geomagnetic Polarity Time Scale. In: Gradstein, F.M., Ogg, James G., Schmitz, M.D. & Ogg, G.M. (Eds.). *Geologic Time Scale 2020* (pp. 159-192). Amsterdam: Elsevier. DOI: <https://doi.org/10.1016/B978-0-12-824360-2.00005-X>
- Paul, A., Reijmer, J., Lampart, J., Kinkel, H. & Betzler, C. 2012. Relationship between Late Pleistocene sea-level variations, carbonate platform morphology and aragonite production (Maldives, Indian Ocean). *Sedimentology*, 59, 1640–1658. DOI: <https://doi.org/10.1111/j.1365-3091.2011.01319.x>
- Poultou, S. W., Krom, M. D. & Raiswell, R. 2004. A revised scheme for the reactivity of iron (oxyhydr)oxide minerals towards dissolved sulfide. *Geochimica et Cosmochimica Acta*, 68, 3703–3715. DOI: <https://doi.org/10.1016/j.gca.2004.03.012>
- Purdy, E. G. & Bertram, G. T. 1993. Carbonate Concepts from the Maldives, Indian Ocean. *AAPG Studies in Geology*, 47, 7–55.
- Reid, J. L., 2003. On the total geostrophic circulation of the Indian Ocean: flow patterns, tracers, and transports. *Progress in Oceanography*, 56, 137–186. DOI: [https://doi.org/10.1016/S0079-6611\(02\)00141-6](https://doi.org/10.1016/S0079-6611(02)00141-6)
- Rey, D., Mohamed, K. J., Bernabeu, A., Rubio, B. & Vilas, F. 2005. Early diagenesis of magnetic minerals in marine transitional environments: geochemical signatures of hydrodynamic forcing. *Marine Geology*, 215, 215–236. DOI: <https://doi.org/10.1016/j.margeo.2004.12.001>
- Roberts, A. P. 2015. Magnetic mineral diagenesis. *Earth-Science Reviews*, 151, 1–47. DOI: <https://doi.org/10.1016/j.earscirev.2015.09.010>
- Roberts, A. P., Chang, L., Rowan, C. J., Horng, C.-S. & Florindo, F. 2011. Magnetic properties of sedimentary greigite (Fe₃S₄): An update. *Reviews of Geophysics*, 49. <https://doi.org/10.1029/2010RG000336>
- Roberts, A. P., Pike, C. R. & Verosub, K. L. 2000. First-order reversal curve diagrams: a new tool for characterizing the magnetic properties of natural samples. *Journal of Geophysical Research*, 105, 28461–28475. DOI: <https://doi.org/10.1029/2000JB900326>
- Roberts, A. P. & Weaver, R. 2005. Multiple mechanisms of remagnetization involving sedimentary greigite (Fe₃S₄). *Earth and Planetary Science Letters*, 231, 263–277. DOI: <https://doi.org/10.1016/j.epsl.2004.11.024>
- Robinson, S. G., Sahota, J. T. S. & Oldfield, F. 2000. Early diagenesis in North Atlantic abyssal plain sediments characterized by rock-magnetic and geochemical indices. *Marine Geology*, 163, 77–107. DOI: [https://doi.org/10.1016/S0025-3227\(99\)00108-5](https://doi.org/10.1016/S0025-3227(99)00108-5)
- Rodelli, D., Jovane, L., Giorgioni, M., Siciliano Rego, E., Cornaggia, F., Benites, M., Padua, P., Berbel, G., Braga, E., Ustra, A., Abreu, F. & Roberts, A. 2019. Diagenetic Fate of Biogenic Soft and Hard Magnetite in Chemically Stratified Sedimentary Environments of Mamanguá Ria, Brazil. *Journal of Geophysical Research: Solid Earth*, 124(3), 2313–2330. DOI: <https://doi.org/10.1029/2018JB016576>
- Rodelli, D., Jovane, L., Roberts, A. P., Cypriano, J., Abreu, F. & Lins, U. 2018. Fingerprints of partial oxidation of biogenic magnetite from cultivated and natural marine magnetotactic bacteria using synchrotron radiation. *Environmental Microbiology Reports*, 10, 337–343. DOI: <https://doi.org/10.1111/1758-2229.12644>
- Rowan, C. J. & Roberts, A. P. 2006. Magnetite dissolution, diachronous greigite formation, and secondary magnetizations from pyrite oxidation: Unravelling complex magnetizations in Neogene marine sediments from New Zealand. *Earth and Planetary Science Letters*, 241, 119–137. DOI: <https://doi.org/10.1016/j.epsl.2005.10.017>
- Rowan, C. J. & Roberts, A. P. 2005. Tectonic and geochronological implications of variably timed magnetizations carried by authigenic greigite in marine sediments from New Zealand. *Geology*, 33, 553–556. DOI: <https://doi.org/10.1130/G21382.1>
- Rowan, C. J., Roberts, A. P. & Broadbent, T. 2009. Reductive diagenesis, magnetite dissolution, greigite growth and paleomagnetic smoothing in marine sediments: A new

- view. *Earth and Planetary Science Letters*, 277, 223–235. DOI: <https://doi.org/10.1016/j.epsl.2008.10.016>
- Sagnotti, L., Roberts, A. P., Weaver, R., Verosub, K. L., Florindo, F., Pike, C. R., Clayton, T. & Wilson, G. S. 2005. Apparent magnetic polarity reversals due to remagnetization resulting from late diagenetic growth of greigite from siderite. *Geophysical Journal International*, 160, 89–100. DOI: <https://doi.org/10.1111/j.1365-246X.2005.02485.x>
- Skinner, B. J., Erd, R. C. & Grimaldi, F. S. 1964. Greigite, the thio-spinel of iron; a new mineral. *American Mineralogist*, 49, 543–555.
- Stramma, L., Johnson, G.C., Sprintall, J. & Mohrholz, V. 2008. Expanding Oxygen-Minimum Zones in the Tropical Oceans. *Science*, 320, 655–658. DOI: <https://doi.org/10.1126/science.1153847>
- Swart, P. K. 2000. The oxygen isotopic composition of interstitial waters: Evidence for fluid flow and recrystallization in the margin of the Great Bahama Bank. *Proceedings of the Ocean Drilling Program, Scientific Results*, 166. DOI: <https://doi.org/10.2973/odp.proc.sr.166.130.2000>
- Till, J. L. & Nowaczyk, N. 2018. Authigenic magnetite formation from goethite and hematite and chemical remanent magnetization acquisition. *Geophysical Journal International*, 213, 1818–1831. DOI: <https://doi.org/10.1093/gji/ggy083>
- Tjallingii, R., Röhl, U., Kölling, M. & Bickert, T. 2007. Influence of the water content on X-ray fluorescence core-scanning measurements in soft marine sediments. *Geochemistry, Geophysics, Geosystems*, 8. DOI: <https://doi.org/10.1029/2006GC001393>
- Torii, M., Fukuma, K., Horng, C.-S. & Lee, T.-Q. 1996. Magnetic discrimination of pyrrhotite- and greigite-bearing sediment samples. *Geophysical Research Letters*, 23, 1813–1816. DOI: <https://doi.org/10.1029/96GL01626>
- Weiss, R. F., Broecker, W. S., Craig, H. & Spencer, D. 1983. *GEOSECS Indian Ocean Expedition: Hydrographic data 1977-1978*. Washington, National Science Foundation.
- Wasilewski, P. J. 1973. Magnetic hysteresis in natural materials. *Earth and Planetary Science Letters*, 20, 67–72. DOI: [https://doi.org/10.1016/0012-821X\(73\)90140-4](https://doi.org/10.1016/0012-821X(73)90140-4)
- Weltje, G. & Tjallingii, R. 2008. Calibration of XRF core scanners for quantitative geochemical logging of sediment cores: Theory and application. *Earth and Planetary Science Letters*, 274, 423–438. <https://doi.org/10.1016/j.epsl.2008.07.054>
- Wilkin, R. T. & Barnes, H. L. 1997. Formation processes of framboidal pyrite. *Geochimica et Cosmochimica Acta*, 61, 323–339. DOI: [https://doi.org/10.1016/S0016-7037\(96\)00320-1](https://doi.org/10.1016/S0016-7037(96)00320-1)
- Yamazaki, T., Abdeldayem, A.L. & Ikehara, K. 2003. Rock-magnetic changes with reduction diagenesis in Japan Sea sediments and preservation of geomagnetic secular variation in inclination during the last 30,000 years. *Earth, Planets and Space*, 55, 327–340. DOI: <https://doi.org/10.1186/BF03351766>